Inorg. Chem. **2007**, *46*, 6675–6682

Luminescence and Photocatalytic Activity of ZnO Nanocrystals: Correlation between Structure and Property

Yuanhui Zheng,[†] Chongqi Chen,[†] Yingying Zhan,[†] Xingyi Lin,[†] Qi Zheng,*[,†] Kemei Wei,[†] Jiefang Zhu,[‡] and Yingjie Zhu[‡]

National Engineering Research Center of Chemical Fertilizer Catalyst, Fuzhou University, Gongye Road 523, Fuzhou, Fujian 350002, China, and State Key Laboratory of High Performance Ceramics and Superfine Microstructure Shanghai Institute of Ceramics, Chinese Academy of Sciences, Shanghai 200050, China

Received December 14, 2006

Low-dimensional ZnO nanocrystals with controlled size, aspect ratio, and oxygen defects (e.g., type and concentration) are successfully prepared through simple solvothermal and thermal treatment methods. The structure of the as-synthesized samples is characterized by XRD, N_2 physical adsorption, TEM, and IR and XPS spectra. The results show that the aspect ratio and size of the as-synthesized ZnO nanocrystals increase with increasing $[OH^-]/[Zn^{2+}]$; the morphology evolves from nanorod to nanoparticle with an increase in the annealing temperature; the BET surface areas of the corresponding samples decrease during these processes, respectively; and different oxygen defects, which are likely to be oxygen vacancy ($V_o^{\bullet\bullet}$) and interstitial oxygen (O_i''), are formed in our experiments accordingly. With evolution of the structure, IR absorption bands and visible photoluminescence emission peaks of the synthesized ZnO nanocrystals shift and split, which is ascribed to the change of oxygen defects. In addition, it is found that the photocatalytic activity of the synthesized ZnO nanocrystals is mainly dependent on the type and concentration of oxygen defects. The relationship of structure–property and the possible photocatalytic mechanism are discussed in detail.

1. Introduction

The application of semiconductor metal oxides (SMOs) in the production of antireflection coatings, transparent electrodes in solar cells,[1] gas/piezoelectric sensors,[2] varistors, surface acoustic wave devices, semiconductor devices, and microelectronics[3] including electro- as well as photoluminescent devices has triggered much research activity. The structure (e.g., size, morphology, defect, and so on) of SMO materials is pivotal to the above potential applications. For example, it has been reported that materials' properties are heavily dependent on the size and morphology tailored by the chemical preparation conditions.[4−8] In addition, thermal treatment and ion doping of nanomaterials are other important factors for controlling the properties.[9,10] Therefore, investigating the factors that govern properties of nanomaterials (especially SMOs) is an important and indispensable issue in the development of nanomaterials.

ZnO, as one of the most popular n-type SMOs, is a versatile material with a wide band gap (3.37 eV) and large exciton binding energy (60 meV). So far, much effort has been focused on low-dimensional ZnO nanostructures, such as nanowires (nanorods),[11] nanotubes,[12] nanoribbons,[13] tet-

* To whom correspondence should be addressed. E-mail: zhengqi@fzu.edu.cn. Phone: +86-591-8373-1234-8416. Fax: +86-591-8373-8808.
† Fuzhou University.
‡ Chinese Academy of Sciences.

(1) Van de Lagemaat, J.; Frank, A. J. *J. Phys. Chem. B* **2000**, *104*, 4292.
(2) Kummer, A. M.; Hierlemann, A.; Baltes, H. *Anal. Chem.* **2004**, *76*, 2470.
(3) Gordon, R. G.; Becker, J.; Hausmann, D.; Suh, S. *Chem. Mater.* **2001**, *13*, 2463.
(4) Suryanarayana, C.; Koch, C. C. *Non-Equilibrium Processing of Materials*; Pergamon Materials Series; Pergamon Press: New York, 1999.
(5) Choudary, B. M.; Mulukutla, R. S.; Klabunde, K. J. *J. Am. Chem. Soc.* **2003**, *125*, 2020.
(6) Djurišić, A. B.; Leung, Y. H.; Tam, K. H.; Ding, L.; Ge, W. K.; Chen, H. Y., Gwo, S. *Appl. Phys. Lett.* **2006**, *88*, 103107.
(7) Zheng, Y.; Cheng, Y.; Wang, Y.; Bao, F.; Zhou, L.; Wei, X.; Zhang, Y.; Zheng, Q. *J. Phys. Chem. B* **2006**, *110*, 3093.
(8) Zheng, Y.; Cheng, Y.; Wang, Y.; Zhou, L.; Bao, F.; Jia, C. *J. Phys. Chem. B* **2006**, *110*, 8284.
(9) Konta, R.; Ishii, T.; Kato, H.; Kudo, A. *J. Phys. Chem. B* **2004**, *108*, 8992.
(10) Su, X.; Zhang, Z.; Zhu, M. *Appl. Phys. Lett.* **2006**, *88*, 061913.
(11) Cheng, B.; Samulski, E. T. *Chem. Commun.* **2004**, 986.

10.1021/ic062394m CCC: $37.00 © 2007 American Chemical Society
Published on Web 07/10/2007

Table 1. Experimental Conditions and Characterization of the Obtained ZnO Nanocatalysts[a]

catalyst	route	$[OH^-]/[Zn^{2+}]$	annealing temperature (°C)	aspect ratio L/D^a	aspect ratio L/D^b	S_{BET} (m^2/g)
Z20	solvothermal	20	without annealing	1.3	≫5	8.4
Z10	solvothermal	10	without annealing	1.3	≫5	13.3
Z5	solvothermal	5	without annealing	2.0	~5	22.3
Z5-300	thermal	5	300	1.5		19.4
Z5-500	thermal	5	500	1.2		6.9
Z5-700	thermal	5	700	1.0	1.0	2.3

[a] L/D^a and L/D^b (L = length along the [001] direction, and D = diameter along [100] direction) are obtained from XRD and TEM, respectively.

rapods,[14] towerlike,[15] and nanoparticles (including quantum dots),[16] because of their novel electronic, optical, and catalytic properties. Most of them were fabricated by several high-temperature methods such as vapor-phase transport, vapor−liquid−solid growth, vapor-phase epitaxy, and template-assisted techniques, along with some low-temperature routes such as wet chemical reactions and electrochemical techniques. Considering the promising applications of ZnO nanocrystals, we select them as research objects in this work to study and understand the relationship between structure and property.

It is well-known that the existence of defects in a semiconductor would lead to a corresponding defect energy level in the band gap. Therefore, we believe that different types of oxygen defects such as oxygen vacancy and interstitial oxygen in ZnO nanocrystals should result in a change in their photoluminescence (PL) and photocatalytic properties. On the basis of the concept of a material's property being determined by its structure, it is expected to control the nanostructures (e.g., size, morphology, and oxygen defects) of ZnO by using different synthetic technology and/or adjusting experimental conditions, thereby tailoring the properties. However, the challenge of this work is how to obtain different types of oxygen defects in ZnO nanocrystals. In the rational design of experiments, two facile synthetic methods are employed to control the structure. First of all, an ethanol-mediated solvothermal method described earlier by Cheng and Samulski[11] is adopted to fabricate ZnO nanorods with different aspect ratios and sizes by adjusting the molar ratio of $[OH^-]/[Zn^{2+}]$. The oxygen vacancy defects should be generated through the deprivation of surface oxygen using ethanol at high temperature and pressure. The second is the thermal treatment method, in which the as-synthesized samples ($[OH^-]/[Zn^{2+}] = 5$) are selected as starting materials and annealed at different temperatures to control the morphology and interstitial oxygen defects. The PL and photocatalytic properties of the as-prepared samples are investigated in detail. Our experimental results show that the optical and photocatalytic properties of ZnO nanocrystals are dependent on the type and concentration of oxygen defects in the synthesized ZnO nanocrystals.

2. Experimental Section

2.1. Preparation of ZnO Nanocrystals. Materials. Zinc acetate, sodium hydroxide, and alcohol are all of analytical grade and were purchased from Shanghai Chemical Reagent Ltd. without further purification.

Synthesis. Large-scale ZnO nanocrystals have been synthesized through the following two methods, and the corresponding preparation conditions are listed in Table 1. For the solvothermal method, 1 mmol of $Zn(Ac)_2 \cdot 2H_2O$ and a certain concentration of NaOH (e.g., 5, 10, and 20 mmol) were mixed in 30 mL of ethanol, stirred at room temperature for 30 min, and then moved to a Teflon-lined stainless steel autoclave of 50 mL capacity. The sealed tank was put into an oven and heated at 160 °C for 24 h. When the reactions were completed, the autoclave was cooled to room temperature naturally. The white precipitates were collected by filtration, washed with deionized water and ethanol several times, and finally dried in air at 60 °C for 10 h. The samples thus obtained were named as Z5, Z10, and Z20, respectively. For the thermal treatment method, three Z5 samples were used as starting materials and annealed at a given temperature of 300, 500, and 700 °C for 3 h in air, the results of which were denoted as Z5-300, Z5-500, and Z5-700, respectively.

2.2. Characterizations. The powder X-ray diffraction (XRD) patterns of the samples were recorded by a Rigaku-DMAX2500 X-ray diffractometer using Cu Kα radiation ($\lambda = 0.154$ nm) at a scanning rate of 5 °C/min. Microstructures and morphologies were investigated using a JEOL-2010 transmission electron microscope (TEM) working at 200 kV. The surface area was measured by the Brunauer−Emmett−Teller (BET) method using N_2 adsorption at 77 K on a Quantachrome NOVA 4200e apparatus. Infrared (IR) and UV−vis spectra were measured on a Perkin-Elmer Spectrum System 2000 FTIR spectrometer and a UV−vis−NIR spectrometer (Cary-500), respectively. X-ray photoelectron spectroscopy (XPS) measurements were performed on a Phi Quantum 2000 spectrophotometer with Al Kα radiation (1486.6 eV). Room-temperature fluorescent characterization was performed on an Edinbursh F900 with an excitation wavelength of 370 nm. For photocatalytic measurement, 20 mg of each catalyst was suspended in 50 mL of a methyl orange (MO) aqueous solution (5.0×10^{-5} M), and then the mixture was put in a quartz tube and shaken overnight in the absence of light to attain equilibrium adsorption on the catalyst surface. UV irradiation was carried out using a 300 W high-pressure Hg lamp (the strongest emission at 365 nm) cooled by cycling water. After a given irradiation time, about 3.5 mL of the mixture was withdrawn, and the catalysts were separated from the suspensions by filtration through 0.22 μm cellulose membranes. The degradation process was monitored by a Cary-500 spectrometer (measuring the absorption of MO at 463 nm).

(12) Shen, X. P.; Yuan, A. H.; Hu, Y. M.; Jiang, Y.; Xu, Z.; Hu, Z. *Nanotechnology* **2005**, *16*, 2039.
(13) Gao, P. M.; Ding, Y.; Mai, W. J.; Hughes, W. L.; Lao, C. S.; Wang, Z. L. *Science* **2005**, *309*, 1700.
(14) Yang, P.; Yan, H. Q.; Mao, S.; Russo, R.; Johnson, J.; Saykally, R.; Morris, N.; Pham, J.; He, R.; Choi, H. J. *Adv. Funct. Mater.* **2002**, *12*, 323.
(15) Wang, Z.; Qian, X. F.; Yin, J.; Zhu, Z. K. *Langmuir* **2004**, *20*, 3441.
(16) Qian, D.; Jiang, J. Z.; Hansen, P. L. *Chem. Commun.* **2003**, 1078.

3. Results and Discussion

3.1. Formation of ZnO Nanocrystals with Different Sizes, Morphology, and Oxygen Defects. As discussed in the Experimental Section, the final products are prepared by two different methods: solvothermal and thermal treatment methods. When acetic zinc is added into a sodium hydroxide solution and the mixture is agitated for 0.5 h, the white precursor is formed gradually. The chemical reactions for the formation of the ZnO precursor can be formulated as

$$Zn^{2+} + 4OH^- = Zn(OH)_4^{2-} \quad (1)$$

$$Zn(OH)_4^{2-} \rightleftharpoons ZnO + H_2O + 2OH^- \quad (2)$$

When the concentration of OH^- increases, the reaction (eq 2), the chemical equilibrium of which is destroyed, tends to proceed toward the left side. As a result, the small ZnO precursor formed would dissolve through the reverse reaction of eq 2 and then transport to larger ones at high temperature (Ostwald ripening process). Therefore, it is reasonable that if the molar ratio of $[OH^-]/[Zn^{2+}]$ increases, the grain size would increase accordingly. Moreover, it is well-known that ethanol is a weak reducing agent under high temperature and pressure or light irradiation. Thus, when the precursor is treated solvothermally (ethanol as the solvent) at 160 °C for 24 h, the oxygen vacancy should be generated on the surface of ZnO nanocrystals (the deprivation of surface oxygen by ethanol). That is to say, the exposed surface of the synthesized ZnO nanocrystals should be a Zn^{2+} terminal surface, similar to the results presented in our previous study of the α-Fe_2O_3 system.[7] However, when ZnO nanocrystals with a surface oxygen vacancy are treated thermally in air (oxygen-rich conditions) at high temperature, the surface ZnO melts, transports from the amphi-end to the center of the nanorods, and forms the spheroidal nanoparticles. Simultaneously, O_2 molecules in the air tend to be adsorbed on the surface of ZnO nanocrystals, ionized, and then implanted onto the ZnO surface layers during this course. Consequently, the other oxygen defects, namely interstitial oxygen instead of oxygen vacancy, should be formed. The chemical reaction process for the generation of these two kinds of oxygen defects is proposed as follows:

$$ZnO \xrightarrow[\text{solvothermal}]{\text{ethanol}} ZnO_x(1-x)V_o^{\bullet\bullet} \xrightarrow[\text{anneal}]{\text{in air}} ZnO_y(y-x)O_i'' \quad (x < 1, y > 1)$$

It is reasonable that the higher annealing temperature could lead to the change in morphology (nanorod to nanoparticle) and defect type ($V_o^{\bullet\bullet} \rightarrow O_i''$).

3.2. Crystal Structure and Microstructure of ZnO Nanocrystals. The XRD patterns of the samples prepared through solvothermal and thermal treatment methods are shown in Figure 1. All of the diffraction peaks on the curves match the standard data for a hexagonal ZnO wurtzite structure (JCPDS 36-1451), and no characteristic peaks of any impurities are detected in the patterns, which demonstrates that all of the samples have high phase purity. Moreover, no remarkable shift of the diffraction peaks among all of the samples reveals that lattice expansion and/or shrinkage should be neglected. In addition, it is found that the half peak width of the samples synthesized through the solvothermal method without calcinations becomes narrower with an increase of the molar ratio of $[OH^-]/[Zn^{2+}]$ (Z5 → Z20), which implies a pronounced grain growth of ZnO nanocrystals. Their aspect ratios calculated from XRD patterns (L/D > 1, as shown in Table 1) reveal 1D morphology of these samples. However, for the samples synthesized by the thermal treatment route, the full width at half maximum of all of the diffraction peaks except for the (002) peak increases with an increase in the annealing temperature (Z5 → Z5-700), indicating a decrease of the aspect ratio and the morphology evolution from 1D morphology to particle during the annealing process. The BET surface area of the as-prepared samples decreases with the increase in $[OH^-]/[Zn^{2+}]$ or the annealing temperature, as shown in Table 1.

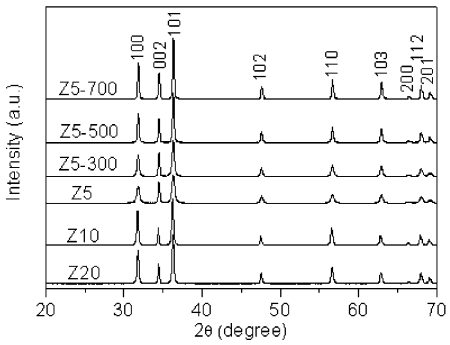

Figure 1. XRD patterns of the samples synthesized under different conditions.

TEM observations confirm the 1D morphology (rodlike) of ZnO nanocrystals synthesized through the solvothermal method under different molar ratios of $[OH^-]/[Zn^{2+}]$, as presented in parts a and b of Figure 2and the Supporting Information (SI-1). It is obvious that the size of the nanocrystals increases with the increase in the molar ratio of $[OH^-]/[Zn^{2+}]$, in agreement with the above XRD results. When a relatively low molar ratio of $[OH^-]/[Zn^{2+}] = 5$ is adopted, a high yield of ZnO nanorods with widths of about 20 nm and lengths of up to about 100 nm (aspect ratio of about 5:1) is obtained, as shown in Figure 2a. A typical high-resolution TEM (HRTEM) image of a single ZnO nanorod (Figure 2b) shows the uniform lattice structure and single-crystalline nature. It is worthwhile to mention that there are not any detectable crystal defects (e.g., microtwins or dislocations) in the ZnO nanorod except for unsaturated bonds on the surface. The spacing between adjacent lattice fringes is 0.256 nm, which is close to the *d* spacing of the (002) plane. The corresponding fast Fourier transform pattern (inset in Figure 2b) is indexed to a hexagonal phase along the $[1\bar{1}0]$ zone axis, indicating the [001] direction (*c* axis) to be the preferential growth direction of ZnO nanocrystals. When the molar ratio of $[OH^-]/[Zn^{2+}]$ is increased further, the grain size of ZnO nanocrystals increases accordingly (Supporting Information, SI-1). In addition, on the basis of the above XRD results, it is concluded that the morphology of ZnO nanocrystals evolves gradually from nanorod to

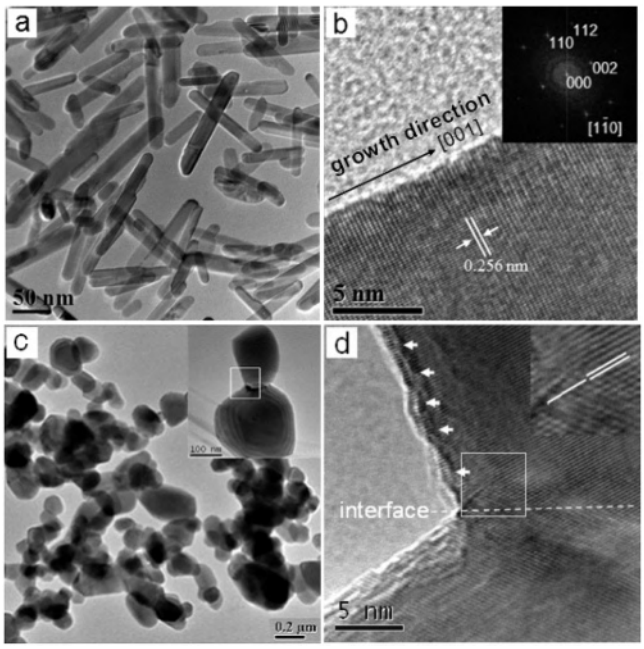

Figure 2. TEM and HRTEM images of the as-synthesized samples (a, b) Z5 and (c, d) Z5-700.

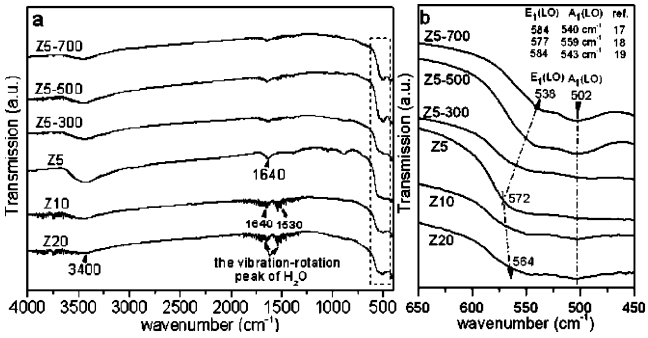

Figure 3. FTIR spectra of the as-synthesized ZnO nanocrystals in the wavenumber ranges of (a) 4000−400 cm^{-1} and (b) 650−450 cm^{-1} (the enlarged FTIR spectra in the rectangular area of Figure 3a). Several reference A_1(LO) and E_1(LO) data were also given for comparison.[17−19]

nanoparticle with an increase in the treatment temperature, which is confirmed by TEM observation of sample Z5-700 (Figure 2c). Figure 2c shows its particle morphology with notable aggregation. A typical HRTEM image (Figure 2d) taken from the squared area in Figure 2c shows that the lattice fringes become curving in surface layers (highlighted by arrows). Moreover, an edge dislocation can be observed, as shown in the inset in Figure 2d. Therefore, there must be many defects on the surface layers of ZnO nanocrystals.

3.3. Surface Structure of ZnO Nanocrystals. Figure 3 exhibits FTIR spectra for the as-synthesized samples. As indicated in Figure 3a, the broad absorptions at about 3400 and 1640 cm^{-1} are assigned to the hydroxyl groups of chemisorbed and/or physisorbed H_2O molecules on the ZnO surface. A strong absorption band revealing the vibrational properties of ZnO nanocrystals is observed for each sample in the range of 650−450 cm^{-1} and magnified in Figure 3b. It is well-known that wurtzite ZnO belongs to the C_{6v} ($P6_3mc$) space group. At the Γ point of the Brillouin zone, there are the following eight optic modes in single-crystalline ZnO: $\Gamma_{opt} = A_1 + A_2 + B_1 + B_2 + 2E_1 + 2E_2$. The A_1, E_1, and E_2 modes are Raman-active. Among these three Raman-active modes, the A_1 and E_1 modes are also IR-active. Moreover, the A_1 and E_1 modes can be polar and hence split into longitudinal- and transverse-optical (LO and TO) components. In Figure 3b, it is obvious that, with an increase of the grain size and annealing temperature, the absorption band splits into two peaks centering at about 570 and 502 cm^{-1}, which are associated with the LO phonons of the E_1 and A_1 modes, respectively. In addition, the vibrational frequency of the E_1(LO) mode shows a remarkable shift of ca. 34 cm^{-1} (Z5 → Z5-700) and ca. 8 cm^{-1} (Z5 → Z20), respectively, whereas the corresponding figure of the A_1-(LO) mode remains almost unchanged for all of the samples. Lu et al. reported that the size-induced lattice variations might lead to an IR absorption red shift.[20] However, on the basis of the XRD results, the effect of lattice variations on the IR absorption shift should be ignored. Then, what is the nature for the evolution of the IR absorption band? In our system, it is suggested that the evolution of the IR absorption band shown in Figure 3 should be ascribed to the variation of the oxygen defect type and density. To explain these phenomena, the calculation of the IR absorption band in the synthesized ZnO nanocrystals is simplified by a physical model—harmonic oscillator. The wavenumber (σ) and vibrational energy (ΔE_v) are expressed as follows:[21]

$$\sigma = \frac{1}{2\pi c}\sqrt{\frac{k}{\mu}} \quad (\mathrm{cm}^{-1}) \tag{3}$$

$$\Delta E_v = \frac{h}{2\pi}\sqrt{\frac{k}{\mu}} \quad (\mathrm{eV}) \tag{4}$$

where c is the velocity of light, k is the bond force constant; μ is the reduced mass, and h is the Planck constant. On the basis of these equations, the position and intensity of the IR absorption peak are determined by the bond force constant (k). For the samples synthesized through the solvothermal method, the concentration of surface $V_o^{\bullet\bullet}$ defects decreases with an increase in the grain size as a result of a reduction in the surface area. Thus, the strength of the Zn−O bond decreases (decrease in the k value), resulting in a shift of the IR absorption peak toward a low wavenumber (Figure 3b, Z5 → Z20). For the samples synthesized through the thermal treatment method, more and more O_i'' defects may be formed on the surface layers of ZnO nanocrystals with an increase in the annealing temperature. Consequently, it goes without saying that this oxygen defect weakens the Zn−O strength (decrease in the k value), which also leads to a shift of the IR absorption peak toward a low wavenumber (Figure 3b, Z5 → Z5-700). Moreover, with variation in the oxygen defects, the intensity of the IR absorption peak ($I \propto E_v$) would change accordingly, which results in a split

(17) Wang, R. P.; Xu, G.; Jin, P. *Phys. Rev. B* **2004**, *69*, 113303.
(18) Decremps, F.; Porres, J. P.; Saitta, A. M.; Chervin, J. C.; Polian, A. *Phys. Rev. B* **2002**, *65*, 092101.
(19) Gao, S.; Zhang, H.; Wang, X.; Deng, R.; Sun, D.; Zheng, G. *J. Phys. Chem. B* **2006**, *110*, 15847.
(20) Lu, L.; Li, L.; Wang, X.; Li, G. *J. Phys. Chem. B* **2005**, *109*, 17151.
(21) George, W. O.; McIntyre, P. S.; Mowthorpe, D. J. *Infrared Spectroscopy*; John Wiley & Sons Inc: New York, 1987; pp 21 and 40.

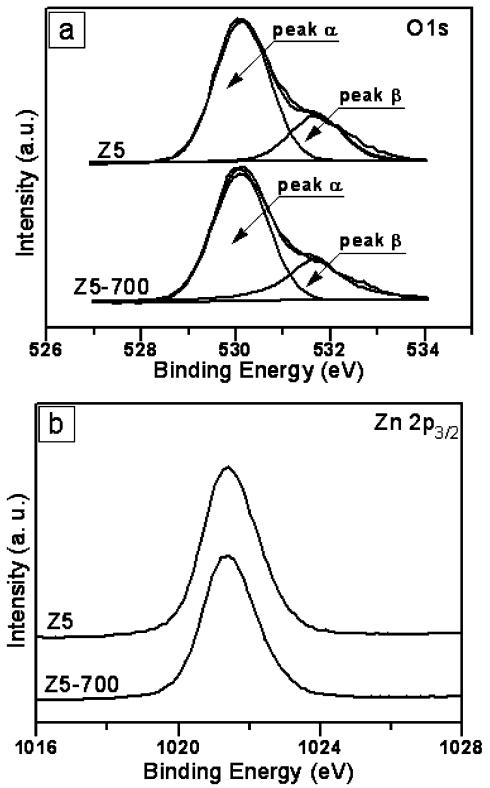

Figure 4. XPS spectra of Z5 and Z5-700 samples: (a) O 1s and (b) Zn $2p_{3/2}$. The binding energies are calibrated using that of C 1s (284.8 eV).

of the IR absorption peak of ZnO nanocrystals. According to the IR peak shifting and splitting degrees of Z20 and Z5-700 samples, it is concluded that the density of oxygen defects for Z5-700 should be much greater than that for Z20. In addition, it is noticeable that the vibrational frequencies of the A_1(LO) and E_1(LO) modes in our samples are much smaller than those reported in the literature[17−19] (shown in Figure 3b).

The surface structures of the Z5 and Z5-700 samples are also investigated by XPS, and the corresponding experimental results are shown in Figure 4 and summarized in the Supporting Information (SI-2). In Figure 4a, the O 1s profiles can be fitted to two peaks (α and β), indicating two different kinds of O species in the samples. The peaks α and β should be associated with the lattice oxygen (O_l) of ZnO[22,23] and chemisorbed oxygen (O_a) caused by a surface hydroxyl group,[24] respectively. The symmetric peaks appearing in Figure 4b are attributed to Zn $2p_{3/2}$.[23] The calculated O_l/Zn ratios are 0.93 and 1.27 for Z5 and Z5-700, which reveals oxygen deficiency and excess oxygen in these samples, respectively.

3.4. Optical Properties and Energy Band Structure. The room-temperature UV−vis absorption spectra of the as-prepared ZnO samples are shown in Figure 5a. One can see

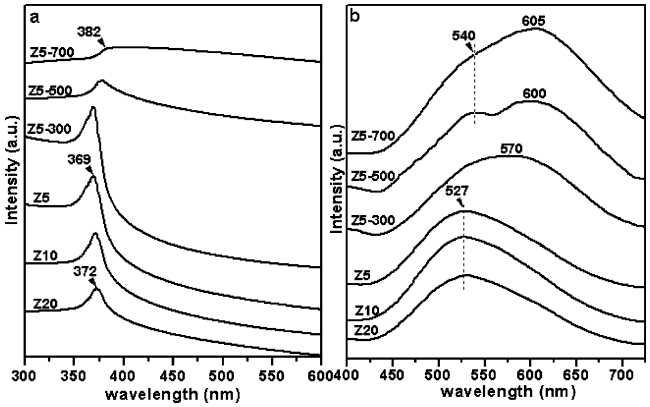

Figure 5. Room-temperature (a) UV−vis absorption and (b) visible PL spectra of the as-synthesized samples.

that the absorption curves are very similar for solvothermal-synthesized samples. The absorption spectra of these samples have a narrow absorption peak located at about 370 nm, which is almost the same as the value of its corresponding bulk. With an increase in the grain size, the absorption peak shifts slightly toward red (Z5 → Z20, only 3 nm). However, for the samples synthesized through the thermal treatment method, the absorption peak shifts toward red about 13 nm (Z5 → Z5-700), which may relate to the change in their morphology. In addition, it is interesting to find that, with an increase in the annealing temperature adopted for the Z5 sample, the band-edge absorption begins at a larger wavelength (Z5 → Z5-700), suggesting that more defects exist in these samples.

The visible PL spectra of the as-prepared samples (Figure 5b) show the evolution of a broad band between 425 and 700 nm. It is reported that this green and/or orange visible luminescence are/is related to deep defect levels located in the gap.[25] Apart from this emission band, there is also a very weak emission peak at 390 nm resulting from free-exciton annihilation (Supporting Information, SI-3). When $[OH^-]/[Zn^{2+}]$ is varied from 5 to 20, the luminescence emission peak of the samples (Z5, Z10, and Z20) synthesized through the solvothermal method remains unchanged and centers at around 527 nm. However, when different annealing temperatures are adopted for the Z5 samples, the corresponding emission peak shifts toward red from 527 nm (green) to 605 nm (orange) with an increase in the annealing temperature. When the sample is annealed at 300 °C, a broad band with a maximum emission intensity at 570 nm is observed. Interestingly, when the annealing temperature is increased further, two emission peaks centered at 540 and 560 nm are observed in the Z5-500 sample (annealed at 500 °C). Moreover, when the annealing temperature is finally increased to 700 °C, there is a broad emission band with one green (a shoulder peak at about 540 nm) and one orange (a main peak at 605 nm) component in the visible region. The peak position of this orange component is the same as the

(22) Peng, W.; Qu, S.; Cong, G.; Wang, Z. *Cryst. Growth Des.* **2006**, *6*, 1518.
(23) Moudler, J. F.; Stickle, W. F.; Sobol, P. E.; Bomben, K. D. *Handbook of X-ray Photoelectron Spectroscopy*; Perkin-Elmer: Eden Prairie, MN, 1992.
(24) Jing, L.; Xu, Z.; Shang, J.; Sun, X.; Cai, W.; Guo, H. *Mater. Sci. Eng., A* **2002**, *332*, 356.
(25) Greene, L. E.; Law, M.; Goldberger, F. K.; Johnson, J. C.; Zhang, Y.; Saykally, R. J.; Yang, P. D. *Angew. Chem., Int. Ed.* **2003**, *42*, 3031.

value reported by Greene et al. and Cross et al.[25,26] It is worthwhile to note that, despite reports that a new emission peak appeared after annealing in air, the position of the new peak almost remains unchanged when the annealing temperature is higher than 400 °C.[27] On the basis of the above discussion, the corresponding energy level diagram is proposed in the Supporting Information (SI-4).

So far, various visible emissions in pure ZnO nanocrystals such as green, yellow, orange, and red emissions have been reported.[6,28] The origin of these visible emissions is still highly controversial. Take the green emission for example. A number of hypotheses have been proposed, such as a singly ionized oxygen vacancy $V_o^{\bullet}$,[29] a $V_o^{\bullet\bullet}$ center,[30] an oxygen antisite,[31] and a zinc vacancy V_{Zn}.[32] Recently, the theoretical analysis also predicts that ZnO has several kinds of defects, such as an oxygen antisite, an oxygen vacancy, a zinc vacancy, an interstitial oxygen, and an interstitial zinc,[31,33−38] which are summarized by Djurišić and Leung.[39] Generally, the green emission is typically associated with oxygen deficiency (e.g., excess Zn^{2+} ions or $V_o^{\bullet\bullet}$ defects) and the orange emission is associated with excess oxygen (e.g., O_i or O_i' defects).[6,40−42] According to the HRTEM, IR, and XPS results as well as the assignments of defects in these literatures, these suggest that the defects formed in our system are likely to be due to an oxygen vacancy ($V_o^{\bullet\bullet}$) and an interstitial oxygen (O_i''). On the basis of the HRTEM analysis (Figure 2b), no detectable defects are observed in the bulk of the ZnO nanocrystals, so the unsaturated bonds of Zn^{2+} ions located on the ZnO surface should be the main defects (there are almost no other defects), which results in the green emission (at 527 nm). Thus, it is reasonable that the luminescence emission peak position remains unchanged with an increase in the ZnO nanocrystal size (decreasing BET surface area). In addition, it is notable that this kind of green emission (at about 527 nm) of ZnO nanocrystals is also found in other synthesis systems, where some reagents such as *N*,*N*-dimethylformamide, dimethyl sulfoxide, and poly(ethylene glycol) are adopted as the unexpected reducing agents.[43,44] Therefore, it is believed that reducing agents may be helpful for the formation of oxygen vacancy defects ($V_o^{\bullet\bullet}$) under certain conditions. In addition, when a Z5 sample is annealed at a given temperature, the interstitial oxygen defects should increase gradually on the surface layers of ZnO nanocrystals, in agreement with the HRTEM observation of the Z5-700 sample. The higher the annealing temperature that is adopted, the more interstitial oxygen defects should be generated and the more surface oxygen vacancy defects should be eliminated (the competition between $V_o^{\bullet\bullet}$ and O_i'' defects). Because the above two different point defects are competing with each other during the annealing process, the overlap of the two emission peaks at 527 and 605 nm will lead to the visible emission peak shifting and/or splitting.

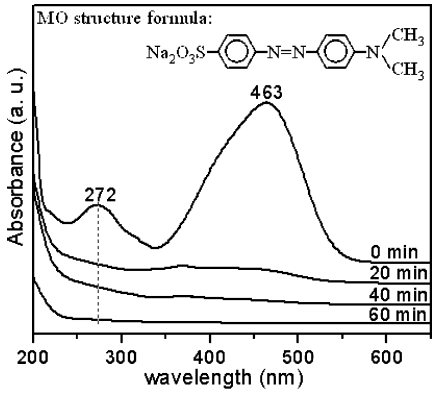

Figure 6. Time-dependent absorption spectra of an MO aqueous solution in the presence of a 20 mg sample of Z5 after UV irradiation.

3.5. Photocatalytic Activities and Mechanism. To understand the relationship between the structure and photocatalytic property of ZnO nanocrystals, the photocatalytic activity of the as-synthesized samples has been investigated by choosing the degradation of MO (its structure formula is inserted in Figure 6). Time-dependent UV−vis absorption spectra of the photocatalytic degradation of MO in the presence of the Z5 sample are recorded, as shown in Figure 6. It is obvious that the absorbance for the maximum peak at 463 nm decreases and shifts toward blue, suggesting the occurrence of the destruction of MO and the formation of some intermediates. When the solution is exposed to UV light for 60 min, the absorption peaks in the curve almost disappear (the MO solution decolorizes completely). To assess the nature of the degradation process, the above products are further analyzed by LC-MSD. The results show that it is a gradual mineralization process (Supporting Information, SI-5). Blank experiments performed without any ZnO catalysts or illumination show that there is no shift in the absorption peak and little change in absorbance at 463 nm (Supporting Information, SI-6), indicating that the catalyst and light are essential for photocatalytic degradation.

The photocatalytic activity of the samples prepared through solvothermal and thermal treatment methods is shown in

(26) Cross, R. B. M.; De Souza, M. M.; Sankara Narayanan, E. M.; *Nanotechnology* **2005**, *16*, 2188.
(27) Tam, K. H.; Cheung, C. K.; Leung, Y. H.; Djurišić, A. B.; Ling, C. C.; Beling, C. D.; Fung, S.; Kwok, W. M.; Chan, W. K.; Phillips, D. L.; Ding, L.; Ge, W. K. *J. Phys. Chem. B* **2006**, *110*, 20865.
(28) Ong, H. C.; Du, G. T. *J. Cryst. Growth* **2004**, *265*, 471.
(29) Vanheusden, K.; Seager, C. H.; Warren, W. L.; Tallant, D. R.; Voigt, J. A. *Appl. Phys. Lett.* **1996**, *68*, 403.
(30) van Dijken, A.; Meulenkamp, E. A.; Vanmaekelbergh, D.; Meijerink, A. *J. Phys. Chem. B* **2000**, *104*, 1715.
(31) Lin, B.; Fu, Z.; Jia, Y. *Appl. Phys. Lett.* **2001**, *79*, 943.
(32) Zhao, Q. X.; Klason, P.; Willander, M.; Zhong, H. M.; Lu, W.; Yang, J. H. *Appl. Phys. Lett.* **2005**, *87*, 211912.
(33) Zhang, S. B.; Wei, S. H.; Zunger, A. *J. Appl. Phys.* **1998**, *83*, 3192; *Phys. Rev. B* **2001**, *63*, 075205.
(34) Lee, E. C.; Kim, Y. S.; Jin, Y. G.; Chang, K. J. *Phys. Rev. B* **2001**, *64*, 085120.
(35) Kohan, A. F.; Ceder, G.; Morgan, D.; Van de Walle, C. G. *Phys. Rev. B* **2000**, *61*, 15019.
(36) Oba, F.; Nishitani, S. R.; Isotani, S.; Adachi, H.; Tanaka, I. *J. Appl. Phys.* **2001**, *90*, 824.
(37) Limpijumnong, S.; Zhang, S. B.; Wei, S. H.; Park, C. H. *Phys. Rev. Lett.* **2004**, *92*, 155504.
(38) Erhart, P.; Klein, A.; Albe, K. *Phys. Rev. B* **2005**, *72*, 085213.
(39) Djurišić, A. B.; Leung, Y. H. *Small* **2006**, *2*, 944.
(40) Monticone, S.; Tufeu, R.; Kanaev, A. V. *J. Phys. Chem. B* **1998**, *102*, 2854.
(41) Wu, L.; Wu, Y.; Pan, X. Kong, F. *Opt. Mater.* **2006**, *28*, 418.
(42) Studenikin, S. A.; Golego, N.; Cocivera, M. *J. Appl. Phys.* **1998**, *84*, 2287.
(43) Rodriguez-Gattorno, G.; Santiago-Jacinto, P.; Rendon-Vazquez, L.; Nemeth, J.; Dekany, I.; Diaz, D. *J. Phys. Chem. B* **2003**, *107*, 12597.
(44) Liu, J.; Huang, X.; Sulieman, K. M.; Sun, F.; He, X. *J. Phys. Chem. B* **2006**, *110*, 10612.

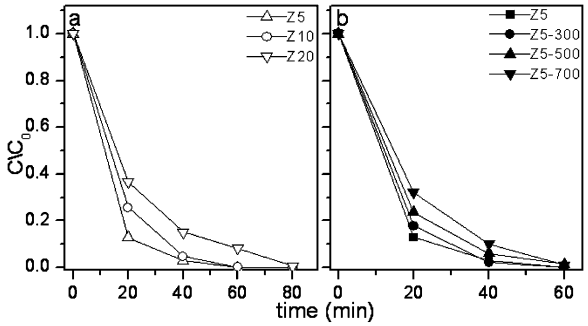

Figure 7. Photodegradation of MO by the samples (a) synthesized under different molar ratios of $[OH^-]/[Zn^{2+}]$ and (b) annealed at different temperatures.

Figure 7. C_0 and C in Figure 7 are the initial concentration after the equilibrium adsorption and the reaction concentration of MO, respectively. It is discovered that the degradation rate for all of the samples is likely to exhibit pseudo-first-order kinetics. When $[OH^-]/[Zn^{2+}]$ is varied from 5 to 20, the photocatalytic degradation rate becomes slower, as shown in Figure 7a. Besides, the photocatalytic degradation rate also becomes slower with an increase in the annealing temperature for ZnO nanocatalysts prepared through the thermal treatment method, as presented in Figure 7b. These results agree with the accepted concept that the catalytic activity is a function of the active available surface area. Comparing parts a and b of Figure 7, we were surprised that, in spite of the smaller BET surface area, the degradation efficiency of the Z5-700 catalyst is much higher than that of the Z20 catalyst.

Naturally, a question comes to us: what causes these differences in photocatalytic activity? To answer this question, it is essential to understand the mechanism of semiconductor photocatalysis. It is generally accepted that, when semiconductor nanocrystals are irradiated by light with energy higher or equal to the band gap, an electron (e^-) in the valence band (VB) can be excited to the conduction band (CB) with the simultaneous generation of a hole (h^+) in the VB. The photoelectron can be easily trapped by electronic acceptors like adsorbed O_2, to further produce a superoxide radical anion (O_2^-), whereas the photoinduced holes can be easily trapped by electronic donors, such as OH^- or organic pollutants, to further oxidize organic pollutants.[45,46] On the basis of our photocatalysis results, it is believed that the difference in photocatalytic activity among all of the samples not only relates to the surface adsorption ability, but also relates to the type and concentration of oxygen defects on the surface and/or surface layers. First, with an increase of $[OH^-]/[Zn^{2+}]$ and the annealing temperature, the grain size increases and the aspect ratio decreases, respectively, resulting in a decrease in the surface area (shown in Table 1). The higher the surface area that the catalyst possesses, the more reactants (e.g., O_2, OH^-, and MO molecules) that should be adsorbed on its surface, thus leading to higher photocatalytic activity. Second, the HRTEM image, IR, XPS, and visible PL spectra suggest the existence of two different

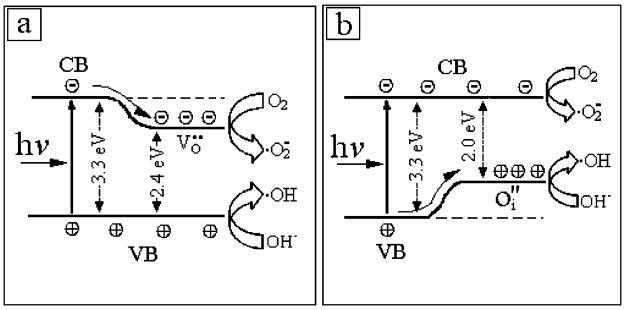

Figure 8. Proposed band structure and photocatalytic mechanism of the as-synthesized ZnO nanophotocatalysts with different oxygen defects (a) oxygen vacancy ($V_o^{\bullet\bullet}$) and (b) interstitial oxygen (O_i'').

kinds of oxygen defects on the surface and/or surface layers. To elucidate the role of oxygen defects on photocatalysis, the proposed schematic photocatalytic mechanism for the photodegradation of MO is illustrated in Figure 8, and the corresponding photocatalytic reaction process can be described by eqs 5−9. The $V_o^{\bullet\bullet}$ defects work as electron

$$ZnO + h\nu \rightarrow e_{cb}^- + h_{vb}^+ \quad (5)$$

$$V_o^{\bullet\bullet} + e_{cb}^- \rightarrow V_o^{\bullet} \quad (6)$$

$$V_o^{\bullet} + O_2 \rightarrow V_o^{\bullet\bullet} + \cdot O_2^- \quad (7)$$

$$O_i'' + h_{vb}^+ \rightarrow O_i' \quad (8)$$

$$O_i' + OH^- \rightarrow O_i'' + \cdot OH \quad (9)$$

acceptors and can trap the photogenerated electrons temporarily to reduce the surface recombination of electrons and holes (eq 6), whereas O_i'' defects sever as photogenerated holes' shallow trappers to restrain the recombination of photogenerated electrons and holes (eq 8). According to these equations, the $V_o^{\bullet\bullet}$ and/or O_i'' defects benefit the efficient separation of electron−hole pairs to minimize the energy-wasteful electron recombination. When the catalysts are immersed in an electrolyte, the band edge of oxygen defects, CBs and VBs bend under the influence of the electric field. Thus, the migration of photogenerated electrons and holes toward different kinds of oxygen defects is reasonable. The excited electrons can easily move to the oxygen vacancies on the surface under the influence of an electric field, as shown in Figure 8a. On the basis of the above discussion, the higher BET surface area (the more $V_o^{\bullet\bullet}$ defects) results in a higher photocatalytic activity (Z5 > Z10 > Z20). However, because there is a potential barrier in ZnO nanocrystals, as presented in Figure 8b, only partial holes could get across it to the interstitial oxygen; thus, the electron−hole pair's separation efficiency of the oxygen vacancy should be higher than that of the interstitial oxygen. Therefore, the photocatalytic activity of Z5 is much better than that of the annealed samples (Z5 > Z5-300 > Z5-500 > Z5-700). In addition, the IR results reveal a higher concentration of O_i'' defects for Z5-700 than that of $V_o^{\bullet\bullet}$ defects for Z20. The net effect of surface adsorption and oxygen defects leads to a higher photocatalytic activity of

(45) Jing, L.; Qu, Y.; Wang, B.; Li, S.; Jiang, B.; Yang, L.; Fu, W.; Fu, H.; Sun, J. *Sol. Energy Mater. Sol. Cells* **2006**, *90*, 1773.
(46) Lin, X.; Huang, T.; Huang, F.; Wang, W.; Shi, J. *J. Phys. Chem. B* **2006**, *110*, 24629.

Z5-700 than that of Z20 (Z5-700 > Z20). It is believed that the results of the present work may provide an efficient approach for designing and fabricating a class of SMO nanomaterials with tunable properties. A more detailed investigation about the effect of other structures such as impurity defects and heterojunctions on the photocatalytic property of ZnO nanocrystals is being carried out.

4. Conclusion

Low-dimensional ZnO nanocrystals with controlled size, aspect ratio, oxygen defect type, and concentration are successfully prepared through simple solvothermal and thermal treatment methods. The relationship between structure and luminescence as well as photocatalytic property is investigated in detail for the first time. The results show that the luminescence and photocatalytic activity of ZnO nanocrystals are mainly dependent on the type and concentration of oxygen defects (e.g., $V_o^{\bullet\bullet}$ and O_i'' defects) formed in our experiments. These defects not only result in the shift and split of the IR absorption band and visible PL emission peak but also increase the charge separation efficiency, thus enhancing their photoactivity.

Acknowledgment. The authors acknowledge the financial support from the Department of Science of the People's Republic of China (Grant 20271012) and the Department of Science & Technology of Fujian Province (Grant 2005H201-2).

Supporting Information Available: TEM images, XPS results, PL spectrum, and LC-MSD data. This material is available free of charge via the Internet at http://pubs.acs.org.

IC062394M